Insights of active sites separation mechanism for highly efficient electrocatalytic N$_2$ reduction to ammonia over glucose-induced metallic MoS$_2$

Ruoqi Liu [a], Hao Fei [a], Jian Wang [b], Ting Guo [a], Fangyang Liu [c], Jiayi Wang [a], Zhuangzhi Wu [a,*], Dezhi Wang [a,*]

[a] *School of Materials Science and Engineering, Central South University, Changsha 410083, China*
[b] *School of Energy and Environment, City University of Hong Kong, Kowloon, Hong Kong Special Administrative Region of China*
[c] *School of Metallurgy and Environment, Central South University, Changsha 410083, China*

ARTICLE INFO

ABSTRACT

Substituting the Haber-Bosch process with electrocatalytic N$_2$ reduction reaction (NRR) is expected to be realized by optimizing the active sites to boost the sluggish N$_2$ adsorption and the hydrogenation process without interference by the thermodynamically favored hydrogen evolution reaction (HER). Herein, a phase engineering strategy for MoS$_2$ toward NRR is reported. The 1T phase are found to enhance the NRR activity with strong N$_2$ adsorption. Then, the active site separation can weaken the competitive adsorption between H$^+$ and N$_2$ reactant on the Mo-edge, improving the NRR selectivity. More importantly, the HER selective basal plane can serve as an H-provider to further accelerate the hydrogenation process of NRR. The optimal MoS$_2$/C-0.4 possesses a high ammonia yield rate of 80.38 μg h^{-1} mg$_{cat.}^{-1}$ and Faradaic efficiency (FE) of 23.76%, outperforming almost all MoS$_2$-based electrocatalysts and beyond. This work sheds light on synchronizing the catalytic activity and selectivity for catalytic reactions.

1. Introduction

The increasing demands for ammonia (NH$_3$) have motivated electrochemical NRR to gain significant attention as a more affordable and sustainable substitute for the conventional Haber-Bosch process [1,2]. Unfortunately, despite many advantages of NRR, it is still seriously hampered by unsatisfactory activity and poor selectivity, mainly due to the inert N≡N triple bond and competitive HER, respectively [3]. Therefore, an ideal electrocatalyst with high catalytic activity and selectivity is essentially desired.

Inspired by nitrogenase, certain transitional metal dichalcogenides [4–6], such as MoS$_2$, have recently been developed as promising electrocatalysts for N$_2$ fixation under ambient conditions [7,8]. However, the limited edge active sites due to the inert basal plane and low conductivity of 2H-MoS$_2$ as a semiconductor seriously suppress the prospect of performance improvements [7,9]. Luckily, compared with 2H-MoS$_2$, metallic 1T-MoS$_2$ can well address these issues with the activated basal plane as well as superior electronic conductivity [10]. Currently, 1T-MoS$_2$ has been frequently reported to exhibit high activity for

ammonia conversion owing to the presence of 1T phase, such as 1T-MoS$_2$/g-C$_3$N$_4$ [11], 1T-MoS$_2$@Ti$_3$C$_2$ [12], SV-1T-MoS$_2$@MoO$_3$ [13], etc. Nonetheless, the deep insights of the selectivity derived from the specific competition between HER and NRR over the aforementioned catalysts have not been clarified, which still has a large room for improvement. In this case, the corresponding competitive behavior is urgently demanded to be further clarified.

In the present work, by a combined approach of theoretical calculation with further experimental support, we proposed the prototype of active site separation over 1T-MoS$_2$ that the Mo-edge and S atoms on the basal plane are selective to NRR and HER, respectively. Such active site separation can well address the competitive issue between NRR and HER on a single absorption site. Additionally, the hydrogenated S atoms can provide a fundamental role in the NRR process as a H-provider because the formed *H can be transferred directly to nearby bound N$_2$ or other nitrogen intermediates, significantly accelerating the NRR process. The optimal MoS$_2$/C-0.4 with 0.4 g of glucose additive presents an exceptional NH$_3$ yield rate of 80.38 μg h^{-1} mg$_{cat.}^{-1}$ and FE of 23.76% at −0.5 V versus reversible hydrogen electrode (vs. RHE), which outperforms

---

almost all MoS$_2$-based NRR electrocatalysts and beyond, demonstrating the dominating contribution of the 1T phase on NRR performance. More noteworthily, the carefully controlled experiments of NRR in various alkali metal salt electrolytes were conducted, in which the FE can be further enhanced to more than 32% by ionically blocking the HER sites on the basal plane of MoS$_2$/C-0.4 in Li$_2$SO$_4$ solution, strongly verifying the proposals in the DFT calculations.

2. Experimental section

2.1. Synthesis of MoS$_2$/C

Firstly, 0.4 g glucose was dissolved into 40 mL deionized water and sonicated for 30 min. Then, 0.3605 g (NH$_4$)$_6$Mo$_7$O$_{24}$·4 H$_2$O and 0.599 g thiourea were added into the solution with continuous stirring for 1 h. The mixture was transferred into a 100 mL Teflon-lined stainless-steel autoclave and maintained at 220 °C for 18 h. After being cooled down, the black product was washed and freeze-dried overnight. The obtained black powder was named MoS$_2$/C-0.4. Moreover, the obtained MoS$_2$/C-0.4 was annealed in a tube furnace at 800 °C for 2 h in Ar to get the A-MoS$_2$/C sample. For comparison, the pure MoS$_2$ without adding glucose was also synthesized under the same conditions and named MoS$_2$/P. Other comparative experiments were also conducted following the same process with various amounts of glucose additive (0.1, 0.2, 0.3, 0.4, and 0.5 g), named MoS$_2$/C-0.1, MoS$_2$/C-0.2, MoS$_2$/C-0.3, MoS$_2$/C-0.4, and MoS$_2$/C-0.5, respectively.

2.2. Characterizations

The X-ray diffraction (XRD) patterns were measured using a D/max-2500 X-ray Diffractometer with a Cu Kα radiation ($\lambda = 0.154$ nm). The scanning electron microscopy (SEM) images were collected on a FEI Sirion 200 scanning electron microscope. The transmission electron microscopy (TEM) images and high-resolution TEM (HRTEM) images were obtained on a JEOL-2100 F transmission electron microscope. The X-ray photoelectron spectroscopy (XPS) was measured on an ESCALAB 250 Xi using Al Kα as the exciting source. The binding energy value of each element was calibrated with C 1s at 284.6 eV. The Raman spectra were acquired using the LabRAMHR-800 (HORIBA, French) at 633 nm.

2.3. Calculations of NH$_3$ formation rate and FE

The FE for the N$_2$ reduction was defined as the amount of electric charge which was used for synthesizing NH$_3$ divided the total charge passed through the electrodes during the electrolysis. The total amount of NH$_3$ was measured using colorimetric methods. Assuming three electrons were needed to produce one NH$_3$ molecule, the FE could be calculated as follows:

$$FE = \frac{3 \times F \times [NH_4^+] \times V}{17 \times Q} \tag{1}$$

The rate of NH$_3$ formation was calculated using the following equation:

$$\text{Ammonia formation rate} = \frac{[NH_4^+] \times V}{m \times t} \tag{2}$$

Where F is the Faraday constant (96485.3 C mol^{-1}), $[NH_4^+]$ is the measured NH$_3$ concentration, V is the volume of the cathodic reaction electrolyte, Q is the quantity of applied electricity, t is the reduction time and m is the catalyst mass."

For more details, please see the Appendix A Supplementary data.

3. Results and discussion

3.1. DFT calculations

Primarily, the origin of the capability improvement of 1T-MoS$_2$ compared with the 2H phase in terms of NRR was explored by density functional theory (DFT) calculations. Fig. S1 concludes the optimum atomic structure for the 1T and 2H phases. Analogous to the 2H phase, the basal plane of the 1T phase is inert towards NRR for not effectively absorbing the N$_2$ molecule (Fig. S2). Taking the N$_2$ adsorption energy and the potential-determining step (PDS) into consideration, the optimum NRR pathway chosen from the several feasible preferred pathways on the 1T phase (Figs. S3–S7) is firstly compared with 2H-MoS$_2$, and the Gibbs free energy diagrams are shown in Fig. 1a. One can see that the 1T-MoS$_2$ possesses dramatically stronger nitrogen adsorption capacity with $\Delta G_{1T-MoS_2}(\text{N-N}\rightarrow\text{N*-N*}) = -2.47$ eV than that of the 2H phase ($\Delta G_{2H-MoS_2}(\text{N-N}\rightarrow\text{N*-N*}) = -1.05$ eV). Furthermore, the PDS is the hydrogenation of N*H$_2$ to produce N*H$_3$ for 1T-MoS$_2$ with an energy barrier of $E_{barrier-1T-MoS_2}^{NRR} = 0.41$ V, which possesses a smaller energy barrier compared with that of 2H-MoS$_2$ (N*-NH→N*-NH$_2$ step, $E_{barrier-2H-MoS_2}^{NRR} = 0.42$ V). The origin of enhanced NRR capacity on the 1T phase is further discussed through the charge density difference (Fig. S8) that a significant charge accumulation region distributes throughout the edges of Mo atoms in the 1T phase compared with the 2H phase, giving the former with more strengthened N$_2$ adsorption and activation capacity [14,15]. The above results indicate that the Mo-edge of the 1T phase owns stronger catalytic activity for NRR than the 2H phase.

Since the competitive relationship of NRR and HER is a key factor that affects the selectivity and activity of catalysts towards NRR, it can be evaluated quantificationally by comparing the Gibbs free energy change in the competitive adsorption step and the energy barrier of the whole reaction, respectively [15,16]. As shown in Fig. 1b, hydrogen atoms can also be adsorbed on the Mo-edge of the 1T phase, and the PDS is the hydrogen desorption step ($E_{barrier-1T-MoS_2}^{HER} = 1.76$ V). When the electrode potential is set as –0.41 V, ΔG (N$_2 \rightarrow$ N*$_2$) = –2.47 eV still remains more negative than ΔG (H$^+$ + e$^- \rightarrow$ H*) = –2.17 eV and ΔG (H$_2$O → H$_2$O*) = –1.68 eV (Fig. S9), which indicates that the Mo-edges of the 1T phase prefer to be covered with nitrogen, instead of hydrogen and water adsorbates. Furthermore, $E_{barrier-1T-MoS_2}^{NRR} < E_{barrier-1T-MoS_2}^{HER}$ implies that the energy barrier of NRR on the Mo-edges of the 1T phase can be more easily overcome. Thus, the Mo-edge of the 1T phase is more selective towards NRR. As for 2H-MoS$_2$, ΔG (H$^+$ + e$^- \rightarrow$ H*) = –1.28 eV is more negative than ΔG (N$_2 \rightarrow$ N*$_2$) = –1.05 eV at an applied electrode potential of –0.42 V, indicating that the Mo-edge of 2H-MoS$_2$ prefers to absorb hydrogen adsorbate, suppressing the NRR process. As a result, the Mo-edge of the 1T phase possesses higher selectivity towards NRR.

In general, the basal plane of 1T-MoS$_2$ has been verified to be the main contributor to the HER activity previously [17,18]. As shown in Figs. S10 and S11, the basal plane of the 1T phase is active towards HER, while that of the 2H phase is in contrast. In the practical NRR process, most protons tend to be absorbed on the basal plane of the 1T phase instead of the Mo-edge because of weaker competitive adsorption of protons on the Mo-edge, as discussed above. Such separation of active sites with selective adsorption, to some extent, can weaken the competitive adsorption between H$^+$ and N$_2$, further improving the NRR selectivity, as demonstrated in our previous work [15]. In this work, we proposed a new role-playing synergistic mechanism based on the active site separation over the 1T phase, as shown in the schematic diagram (Fig. 1c), where the hydrogenated S atoms near the Mo-edge can serve an essential role as H-provider in the NRR since the absorbed *H can be transferred spontaneously with negative ΔG to an absorbed N$_2$ molecule or other nitrogen intermediates on the neighbor Mo-edge (Fig. 1d), such as *^{Mo}N$_2$ + *^{S}H $\rightleftharpoons$ *^{Mo}N$_2$H with a ΔG of –0.25 eV, and then the re-hydrogenated S atoms can be sustainably employed for subsequent
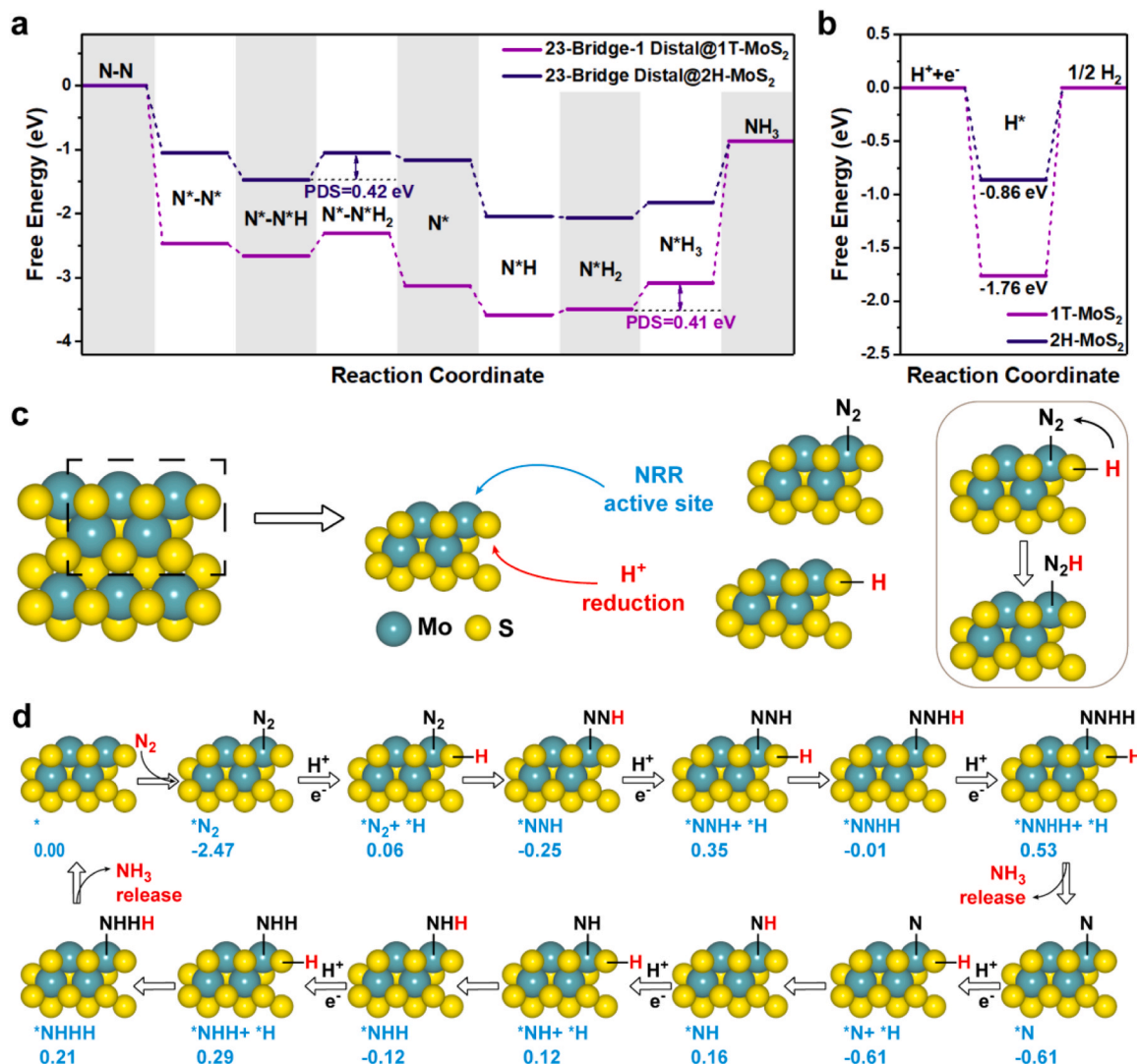
Fig. 1. (a) Gibbs free energy diagrams on the 1T-MoS$_2$ surface along the respective optimum NRR reaction pathway and the 2H-MoS$_2$ surface. The PDS for each reaction pathway is marked. (b) HER Gibbs free energy diagrams on the 1T-MoS$_2$ and 2H-MoS$_2$ surface. The asterisk * in (a) and (b) denotes the atom in the adsorbate, which is bound to the 1T-MoS$_2$ and 2H-MoS$_2$ surfaces. The common intermediates for all reaction pathways on the 1T-MoS$_2$ and 2H-MoS$_2$ surfaces are denoted in black font. (c) The initial model of 1T-MoS$_2$ and the hypothesis that NRR is catalyzed by 1T-MoS$_2$ in a synergetic process in which the Mo edge of 1T-MoS$_2$ acts as a proper NRR active site while the basal plane on pristine behaves as a HER active site. Once N$_2$ is adsorbed, a reduced proton on the edge of the basal plane will subsequently provide hydrogen to hydrogenate the N$_2$. (d) Schematic minimum-energy pathway for electrochemical N$_2$ conversion into NH$_3$ catalyzed by 1T-MoS$_2$. Relative Gibbs free energies are shown in eV at mild conditions.

hydrogenation steps in the NRR. Such synergistic mechanism can further boost the NRR process by the superior activity of Mo-edge on 1T phase, thus facilitating the NH$_3$ formation [19], which will be further verified by the experimental operation in the electrolytes with various alkali metal ions later.

3.2. Characterization of the samples

The synthesis process is schematically depicted in Fig. 2a. We first prepared the high metallic MoS$_2$ induced by the glucose (labeled as MoS$_2$/C) using the hydrothermal method. In this work, the phase content gradient was precisely regulated by various amounts of glucose additive, and the obtained samples were marked as MoS$_2$/C-X, where X represents the amount of glucose additive (i.e., MoS$_2$/C-0.4 represents 0.4 g glucose). In comparison, the pristine MoS$_2$ was prepared without a glucose reactant (MoS$_2$/P). Besides, to obtain the counterpart with pure 2H phase, the MoS$_2$/C-0.4 was further annealed at 800 ℃ under Ar atmosphere (A-MoS$_2$/C). As seen in Fig. S12a, the scanning electron

microscopy (SEM) image of MoS$_2$/P exhibits a nanoflower-like structure consisting of stacked MoS$_2$ nanosheets with a size of 1–2 μm, and the MoS$_2$/C-0.4 in Fig. 2b, S12c and d show the similar morphology but is comprised of distinctly smaller particles with a lateral size of 200–400 nm, further proved by the transmission electron microscopy (TEM) image in Fig. 2c, which may be ascribed to the limited growth of MoS$_2$ crystal owing to the presence of glucose [20]. In addition, the high-resolution TEM (HRTEM) image of MoS$_2$/P in Fig. S12b displays a multilayer structure with an interlayer distance of about 0.62 nm and a thickness of 14 layers, while the MoS$_2$/C-0.4 shows an expanded inter-layer distance of 0.95 nm but fewer layers of nanosheets in comparison (Fig. 2d), further implying the presence of the intercalating ions or molecules and the confined growth caused by the carbon layer, respectively [21–24]. Moreover, the HRTEM image (Fig. 2e) evidences the co-existence of octahedral 1T phase and trigonal 2H phase in MoS$_2$/C-0.4, which are further shown distinctly in Fig. 2f and g [15,25, 26]. The TEM mapping images (Fig. S13) reveal that Mo, S, and C elements are homogeneously distributed in MoS$_2$/C-0.4.
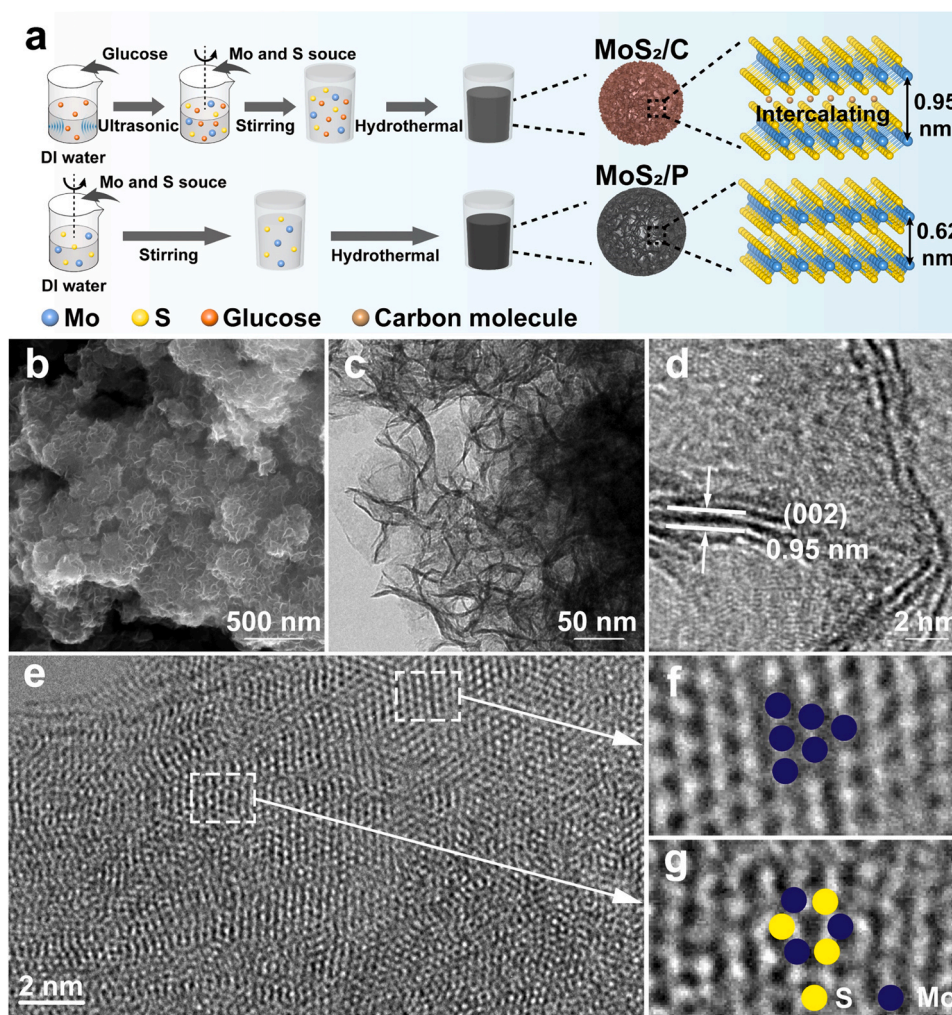
Fig. 2. (a) Synthesis schematic illustration of MoS_2/C and MoS_2/P. (b) SEM, (c) TEM, and (d, e) HRTEM images of MoS_2/C-0.4. (f, g) images of the region enclosed by the white rectangle of (e).

Fig. 3a represents the X-ray diffraction (XRD) patterns for MoS_2/P, A-MoS_2/C, and MoS_2/C-0.4. The characteristic peaks of MoS_2/P at 14.4°, 32.7°, 39.5°, and 58.3° are well matched with (002), (100), (103), and (110) reflections of the standard MoS_2 (JCPDS No. 37–1492), respectively. Compared with that of MoS_2/P, the (002) peak of MoS_2/C-0.4 splits into a $(002)_{new}$ peak and a $(004)_{new}$ peak at 9.0° and 17.6°, respectively, where the latter may be regarded as the second-order diffraction peak of the former since their 2θ values approximately display a diploid relationship, as also observed previously [20,27,28]. Remarkably, the $(002)_{new}$ peak of MoS_2/C-0.4 with a smaller angle compared to that of MoS_2/P indicates the expanded interplanar distance (9.85 Å according to the Bragg equation) assigned to the contribution of the intercalating species, which is in accordance with the HRTEM results in Fig. 2d and other intercalated MoS_2 [29–31]. After annealing, the A-MoS_2/C possesses analogous peak distribution to MoS_2/P, suggesting the reversely transferred phase structure from 1T to the stable 2H phase. Note that the weaker (002) peak of A-MoS_2/C compared with MoS_2/P may be mainly caused by the shielding effect of the carbon layers on the surface and the few-layered structure [20]. The characteristic peaks in Raman spectra (Fig. 3b) of MoS_2/P and MoS_2/C-0.4 at 148, 218, 286, and 336 cm^{-1} are referred to the J_1, J_2, E_{1g}, and J_3 vibration modes of 1T-MoS_2, respectively, undoubtedly justifying the presence of 1T phase [32–34]. Furthermore, there is almost no obvious signal of the A_{1g} peak in MoS_2/C-0.4, showing a relatively pure 1T phase induced by glucose. In comparison, the A-MoS_2/C only exhibits two dominant Raman peaks

of E_{2g}^1 and A_{1g} modes at nearly 375 and 404 cm^{-1}, respectively [35,36], further proving the transformation from 1T to 2H phase after calcination. Moreover, two peaks at approximately 1369 and 1591 cm^{-1} of the MoS_2/C-0.4 and A-MoS_2/C, which belong to the D and G bands of glucose-derived carbon, provide further evidence of their hybrid structure [37,38]. The calculated peak intensity ratio I_D/I_G of MoS_2/C-0.4 is 1.07, while it is 0.91 in A-MoS_2/C, suggesting the presence of amorphous carbon in MoS_2/C-0.4 and the increasing graphitization degree in A-MoS_2/C after annealing [20].

The X-ray photoelectron spectra (XPS) of MoS_2/P and MoS_2/C-0.4 were collected in Fig. S14, which show a higher peak intensity of C 1s in MoS_2/C-0.4 compared with that of MoS_2/P, indicating a relatively high content of carbon induced by glucose in MoS_2/C-0.4. As displayed in the Mo 3d spectra (Fig. 3c), two peaks located at 232.7 and 229.5 eV in MoS_2/C-0.4 are assigned to the Mo $3d_{5/2}$ and $3d_{3/2}$ peak derived from the 2H phase [20,39], whereas another doublet observed at 231.7 and 228.5 eV indicate the appearance of 1T phase [10,18,30]. In the S 2p spectra (Fig. 3d), two characteristic peaks at 160.5 and 161.8 eV for MoS_2/C-0.4 can be attributed to S $2p_{3/2}$ and $2p_{1/2}$ of 1T-MoS_2, respectively, while the other two peaks with binding energies of 161.5 and 162.8 eV should be assigned to 2H-MoS_2 [40]. Besides, the standard peak distribution of the 2H phase over A-MoS_2/C in both Mo 3d and S 2p regions with sharp shape further confirms the reverse phase transition from 1T to 2H phase with higher crystallinity, consistent with the XRD and Raman results. In terms of the deconvoluted peaks area ratio in the
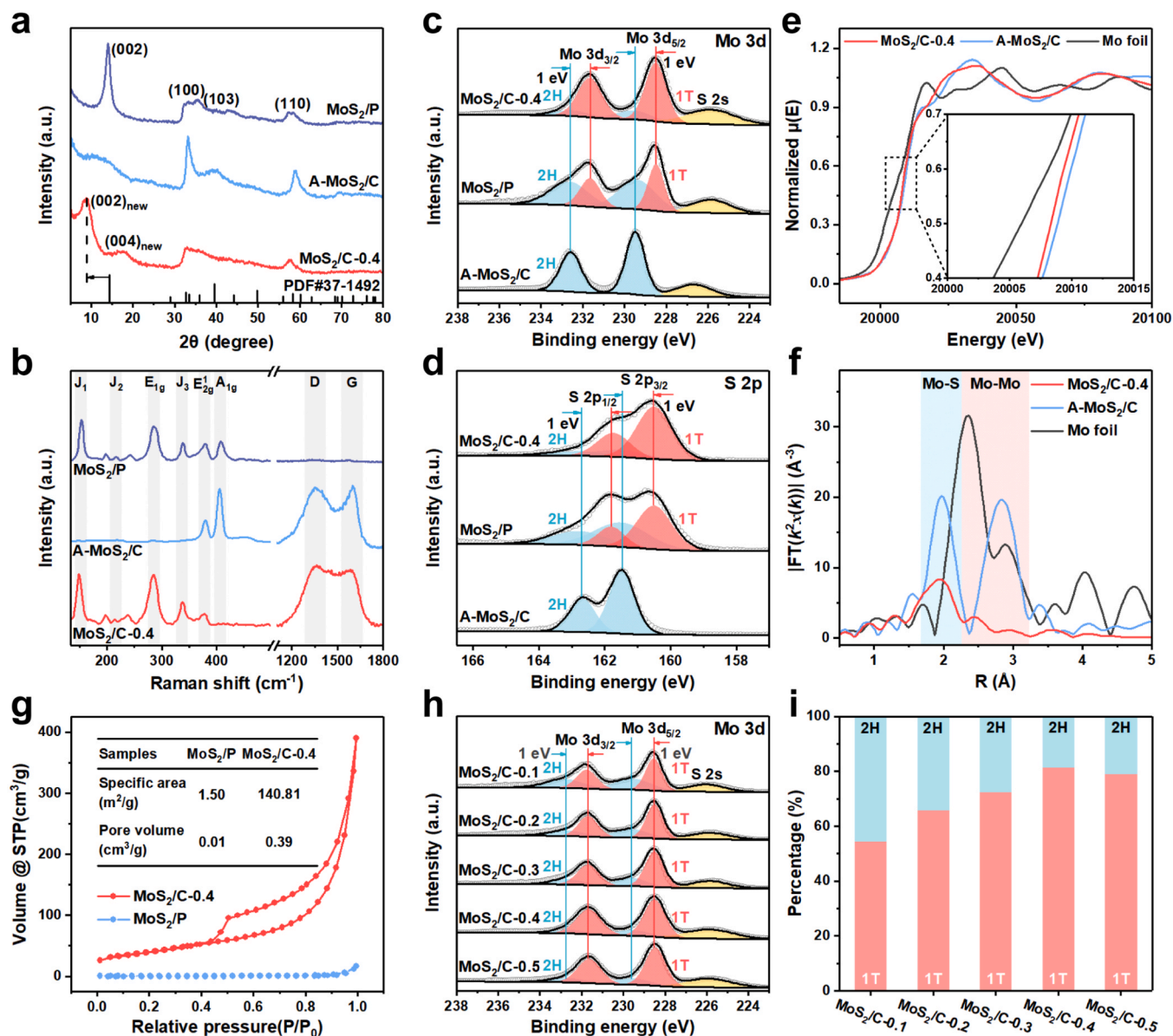
Fig. 3. (a) XRD patterns, (b) Raman spectra, XPS spectra in (c) Mo 3d and (d) S 2p regions over MoS_2/P, MoS_2/C-0.4, and A-MoS_2/C. XAFS results of MoS_2/C-0.4 and A-MoS_2/C samples: (e) Normalized XANES spectra and (f) the corresponding Fourier transform of Mo K-edge EXAFS spectra. (g) N_2 adsorption and desorption isotherms of MoS_2/P and MoS_2/C-0.4. (h) XPS spectra of Mo 3d of MoS_2/C-0.1, MoS_2/C-0.2, MoS_2/C-0.3, MoS_2/C-0.4, and MoS_2/C-0.5. (i) Relative fractions of 1T and 2H phases of MoS_2/C-0.1, MoS_2/C-0.2, MoS_2/C-0.3, MoS_2/C-0.4, and MoS_2/C-0.5.

Mo 3d region, the content of 1T phase in MoS_2/C-0.4 was calculated to be 81.45%, much larger than that of MoS_2/P (40.13%), revealing the boosted glucose-induced phase transition from 2H to 1T [20]. Further investigation of the C 1s and O 1s spectra of MoS_2/C-0.4 (Fig. S15a and b) demonstrates that the C species in the sample is mainly the amorphous carbon, and the edge of the amorphous carbon may bond with some organic groups, which can also be observed in previous literature using the same method to prepare the 1T-MoS_2 [20]. Besides, based on the expanded interlayer distance of MoS_2/C-0.4 in the TEM and XRD results (Figs. 2d and 3a), some of the C species exist in the interlayer of MoS_2 as the intercalating molecules. And from the TEM images in Fig. S15c, one can see that the C species also exists on the surface of the particles, thus causing the confined growth of the MoS_2 nanosheets (Fig. 2b and S12). Moreover, from the TEM-EDX measurement in Fig. S15d, the content of carbon and MoS_2 in the sample is about 48.11 and 45.94 wt%, respectively.

Furthermore, the coordination structures and valence states of the

samples are investigated by the X-ray absorption near-edge structure (XANES) and extended X-ray absorption fine structure (EXAFS). The Mo K-edge XANES spectra (Fig. 3e) show that the MoS_2/C-0.4 presents a low-E shift compared with A-MoS_2/C, suggesting a lower chemical state of Mo in 1T phase MoS_2, as a result of the electron injection from the intercalated species to the MoS_2 slab [10,41,42]. Fig. 3f and S16 depict the radial structural functions (RSFs) of Mo K-edge for the two samples. It reveals that the FT curves of the A-MoS_2/C are characterized by two main peaks at 2.41 and 3.17 Å, corresponding to the nearest Mo-S and Mo-Mo bonds, respectively [10]. In contrast, the FT curve of MoS_2/C-0.4 indicates that the second peak related to the Mo-Mo bond shows a noticeable shift from 3.17 to 2.75 Å. Meanwhile, the intensity of two peaks in A-MoS_2/C obviously increases compared with MoS_2/C-0.4 after annealing, manifesting the declined coordination number of Mo-S and Mo-Mo bonds in MoS_2/C-0.4 (Table S1) [43,44], which is attributed to the distorted octahedral coordination induced by the lattice rotation during the phase transition from the 2H to 1T phase in the material

synthesis [27]. Fig. 3g shows the N_2 adsorption/desorption isotherms and pore diameter distributions. The specific surface area of Bruauer-Emmett-Teller (S_{BET}) are 1.50 and 140.81 m^2 g^{-1}, and the corresponding pore volume (V_{pore}) are 0.01 and 0.39 cm^3 g^{-1} for the MoS_2/P and MoS_2/C-0.4, respectively, which can be mainly attributed to the presence of carbon and partially derived from the dramatically reduced particle size of MoS_2/C-0.4 as revealed in Fig. 2b, S12a, and S15c. The A-MoS_2/C shows the highest BET value and pore volume among the three samples (Fig. S17), which may be attributed to the structural changes induced by the phase transfer for 1T-MoS_2 and the graphitization for the carbon layers, indicating that the larger BET specific surface area and the more porous structure of the MoS_2/C-0.4 than those of MoS_2/P are mainly caused by the smaller particle size instead of the enlarged interlayer distance of MoS_2.

In order to explicitly probe the growth mechanism of MoS_2 crystal with glucose addition, we produced various samples by regulating the amount of glucose. Fig. S18 shows the XRD patterns of MoS_2 prepared with different glucose additive amounts from 0.1 to 0.5 g. It is obvious that the (002) peak of MoS_2 shifts to lower degrees with the increased glucose, indicating more expanded interlayer spacing caused by more carbonized particles derived from glucose. Besides, the XPS analysis in Fig. 3h and i indicate the content of the metallic 1T phase is gradually increased with the increased glucose additive and peaks over MoS_2/C-0.4 and then keeps maintained, demonstrating the induced formation of the metallic 1T phase achieves saturated with superfluous glucose additive. The SEM images in Fig. S19 show that the lateral size of MoS_2 particles becomes smaller with the increased glucose amount due to the increased crystal growth limitation, but when the addition of glucose rises to 0.5 g, the MoS_2 matrix suffers a partial structural collapse and then aggregates into a larger bulk. As discussed above, during the nucleation and growth of crystals, some of the carbonized particles derived from glucose can be inserted into the interlayers of MoS_2, resulting in the broadened layer distance as well as the formation of the metallic 1T phase.
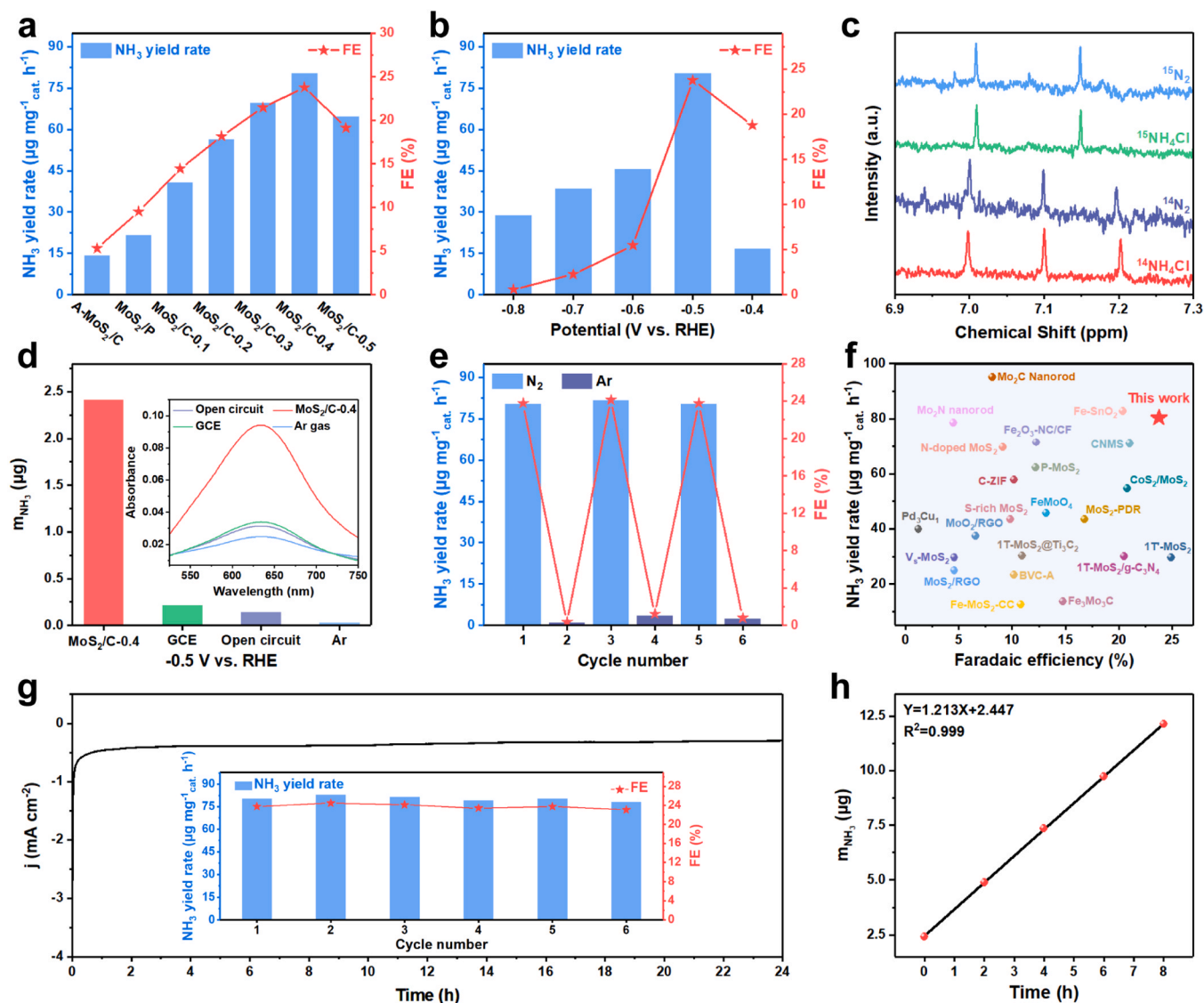

Fig. 4. (a) Comparison of properties (NH_3 yield rates and FEs) at −0.5 V vs. RHE over various catalysts under the same conditions. (b) The properties of MoS_2/C-0.4 at various potentials. (c) ^{1}H NMR (500 MHz) spectra of solution after electrocatalytic N_2 fixation using MoS_2/C-0.4 as the electrocatalyst in the $^{14}N_2$ or $^{15}N_2$ atmosphere. (d) Amount of NH_3 generated after charging at −0.5 V for 2 h under various conditions. The inset is the UV–vis absorption spectra of the electrolytes stained with an indophenol indicator. (e) NH_3 yield rates and corresponding FEs of MoS_2/C-0.4 with switching 2 h cycles between N_2- and Ar-saturated electrolytes. (f) Comparison of NH_3 yields and FE values of MoS_2/C-0.4 with other reported catalysts. (g) Time-dependent current density curve of MoS_2/C-0.4 at −0.5 V for 24 h. The inset is the stability test of MoS_2/C-0.4 during repeated NRR for six cycles at −0.5 V. (h) Curve of ammonia yield vs. reaction time at −0.5 V over MoS_2/C-0.4.

3.3. NRR performance of the samples

Under the ambient conditions, the as-synthesized catalyst was dropped on a glassy carbon electrode and served as a working electrode for the NRR in a three-compartment cell separated by a proton exchange membrane. Before NRR, the possible presence of NH_3/NO_x contaminants in the feeding N_2 was carefully removed by sufficient purification using an acid trap (0.05 M H_2SO_4) and an alkaline trap (0.1 M KOH), respectively [45–47]. The corresponding calibration curves of the generated NH_3 estimated by the indophenol blue method and the possible by-product (N_2H_4) estimated by the Watt and Chrisp method are illustrated in Figs. S20 and S21, respectively [15]. Fig. 4a and S22 display the NH_3 yield rates and FEs of as-obtained catalysts at various potentials. One can see that the NRR performance is enhanced with the increased glucose amount and peaks at MoS_2/C-0.4, and then falls down. In addition, the MoS_2/C-0.4 presents a NH_3 yield rate of 80.38 µg h^{-1} mg$_{cat.}^{-1}$ and FE of 23.76% at −0.5 V vs. RHE, far higher than that of MoS_2/P (NH_3 yield rate: 21.48 µg h^{-1} mg$_{cat.}^{-1}$, FE: 9.53%) with less 1T phase and A-MoS_2/C (NH_3 yield rate: 14.27 µg h^{-1} mg$_{cat.}^{-1}$, FE: 5.33%) without 1T phase, respectively, indicating that the 1T phase plays a dominant role in electrocatalytic NRR process. Linear sweep voltammetry (LSV) measurement of MoS_2/C-0.4 performed in N_2-saturated 0.1 M K_2SO_4 solution possesses a higher current density than that in Ar-saturated solution, demonstrating that NRR occurs at the specific potential range owing to the extra contribution of the multiple electronic steps for NRR (Fig. S23a) [48,49]. The average NH_3 yield rates and FEs of MoS_2/C-0.4 at potentials varying from –0.4 to –0.8 V were evaluated (Fig. 4b and S24), where the time-current density curves show minor variations at each given potential (Fig. S23b), exhibiting superior durability during the catalytic process. Note that since the competitive HER becomes more predominant below –0.5 V, both NH_3 yield rates and FEs are significantly reduced [15,23]. Other quantified methods consist of Nessler's reagent methods, ion chromatography (IC) methods, and quantified nuclear magnetic resonance (NMR) methods for redetermining the NH_3 yield rate have also been performed in this work to check out the reliability of the indophenol blue method [50–52], as displayed in Figs. S25–S27, further confirming the validity of the data. Besides, in order to discover the origin of the N species in the generated NH_3, ^1H isotopic labeling NMR experiments were conducted (Fig. 4c). The characteristic triplet peaks of $^{14}NH_4^+$ are detected when $^{14}N_2$ gas is supplied, while the doublet assigned to $^{15}NH_4^+$ can be observed using $^{15}N_2$ as the feeding gas [53]. Further quantitative NRR evaluation in Fig. S28 provides strong evidence that the feeding N_2 gas serves as the sole source for N species in the generated NH_3. On this basis, extra control experiments were carefully conducted (Fig. 4d and e) [54–56]: (1) MoS_2/C-0.4 in a N_2-saturated 0.1 M K_2SO_4 solution at an open circuit potential for 2 h; (2) MoS_2/C-0.4 in an Ar-saturated 0.1 M K_2SO_4 solution at –0.5 V for 2 h; (3) a bare GCE in a N_2-saturated 0.1 M K_2SO_4 solution at –0.5 V for 2 h; (4) MoS_2/C-0.4 at –0.5 V with alternating 2 h cycles between N_2- and Ar- saturated 0.1 M K_2SO_4 solution for 12 h. Only the NRR over MoS_2/C-0.4 in an N_2-saturated 0.1 M K_2SO_4 solution generates a comparable amount of NH_3, further verifying the origin of N species. Noteworthily, the byproduct N_2H_4 was measured by a Watt and Chrisp method (Fig. S29), which demonstrates that there is no N_2H_4 generated during the NRR process. Therefore, such superior NRR activity and selectivity empowered by MoS_2/C-0.4 are favorably compared to almost all state-of-the-art NRR electrocatalysts (Fig. 4f and Table S2 in detail).

Stability can be evaluated by 24 h electrolysis, as shown in Fig. 4g. MoS_2/C-0.4 keeps favorable electrochemical durability with only a minor fluctuation of current density at –0.5 V, as well as both the NH_3 yield rate and FE after six consecutive cycles (the inset in Fig. 4g), which is further supported by the great linear dependency between NH_3 yield and reaction time during the electrolysis process (Fig. 4h). Meanwhile, the XRD, XPS, and TEM results in Fig. S30 further verify the morphological and structural stability, especially the content of the 1T phase of

MoS_2/C-0.4 after the NRR test. Thus, the MoS_2/C-0.4 catalyst indeed exhibits superb electrochemical catalytic activity, selectivity, and stability for NRR.

In detail, we first investigated the enhanced mechanism of the outstanding activities over MoS_2/C-0.4 towards NRR. The electrochemical active surface area (ECSA) derived from the double-layer capacitance (C_{dl}) was collected (Figs. S31 and 5a; Table S3). One can see that the ECSA increases with the increased additive of glucose and achieves the maximum over MoS_2/C-0.4, then drops down (Fig. 5d), implying the strong dependence between the number of active sites and the 1T phase. Besides, the ECSA value of MoS_2/C-0.5 is much lower than that of MoS_2/C-0.4, which is attributed to the shielding effect of carbon layers on active sites derived from the excess glucose, thus leading to the worse NRR performance of MoS_2/C-0.5 than that of MoS_2/C-0.4. Benefiting from more exposed active sites of the 1T phase to absorb N_2 molecules, the MoS_2/C-0.4 possesses a much higher nitrogen temperature-programmed desorption (TPD) signal (150–300 ℃) than MoS_2/P without glucose additive (Fig. 5b), revealing more N_2 absorption. Meanwhile, the MoS_2/C-0.4 also exhibits an extra desorption signal at higher temperatures (300–400 ℃), indicating a stronger N_2 absorption capacity of the 1T phase, which corresponds to the DFT results (Fig. 1a). The corresponding electrical impedance spectroscopic (EIS) measurements (Fig. 5c and d) demonstrate a relatively more efficient electron transfer and boosted electrocatalytic NRR kinetics for MoS_2/C-0.4 owing to the highest content of 1T phase as the metallic nature. In addition, we can see from Fig. 5e, f, and S32 that the evolution of TOF_{NRR} and TOF_{HER} possess strong dependence on the content of the 1T phase, indicating that the presence of the 1T phase can enhance the intrinsic activity of both NRR and HER. Consequently, the enhanced NRR activity of MoS_2/C-0.4 can be attributed to the 1T phase-induced synergetic effects of enhanced intrinsic activity with improved N_2 adsorption, increased number of active sites, and accelerated electron transport kinetics.

To provide evidence for the deduction of active site separation in the DFT calculation and further reveal the enhanced mechanism of the superior NRR selectivity over MoS_2/C-0.4, we constructed MoS_2/C-0.4 for electrocatalytic NRR in K_2SO_4, Na_2SO_4, and Li_2SO_4 solutions, respectively, as shown in Fig. 5g and S33. The NH_3 yield rates of MoS_2/C-0.4 in K_2SO_4, Na_2SO_4, and Li_2SO_4 solutions are found to be decreased in order, while the FEs interestingly show the opposite trend. Meanwhile, the ECSA of MoS_2/C-0.4 in the above three solutions was also tested (Fig. S34), and it was found that the different steric effect of alkali metal ions affects the ECSA of the samples [57]. The MoS_2/C-0.4 in Li_2SO_4 shows the smallest ECSA due to the strongest Li-S interactions [5], indicating that the reduction of ECSA mainly originates from the S sites on the basal plane, which serve as the primary activity contributor on 1T phase for HER, while the Mo-edge sites are not affected [17]. In addition, it can be seen from the LSV curves (Fig. S35) that the current density of MoS_2/C-0.4 in K_2SO_4, Na_2SO_4, and Li_2SO_4 solutions gradually decreases. Besides, to check out the reliability of the obtained FE in the Li_2SO_4 solution, we conducted the NRR measurement at –0.5 V twice, and the corresponding UV–vis spectra and time-current density curves of MoS_2/C-0.4 in the Li_2SO_4 solution are plotted in Fig. S36. One can see that the FE of MoS_2/C-0.4 keeps favorable durability with only a minor fluctuation, strongly confirming the validity of the data. Combined with the respective TOFs of both HER and NRR (Fig. 5h and i), the decline in current density is mainly attributed to more hindered HER by limiting H adsorption due to the strong interaction of alkali metal ions to S atoms on the basal plane of MoS_2/C-0.4, and the suppressed extent is $Li^+ > Na^+ > K^+$. In addition, the hindered H adsorption on the basal plane leads to the unavailability of an H provider for the subsequent NRR hydrogenation step, which also slows down the NRR process at the Mo-edge sites, resulting in a decreasing trend in TOF_{NRR} and therefore a minor decrease in NH_3 yield rates. Such decrease is less than the suppression of HER on the basal plane by alkali metal ions, so the FE inversely increases, and the NRR selectivity of MoS_2/C-0.4 can be improved to more
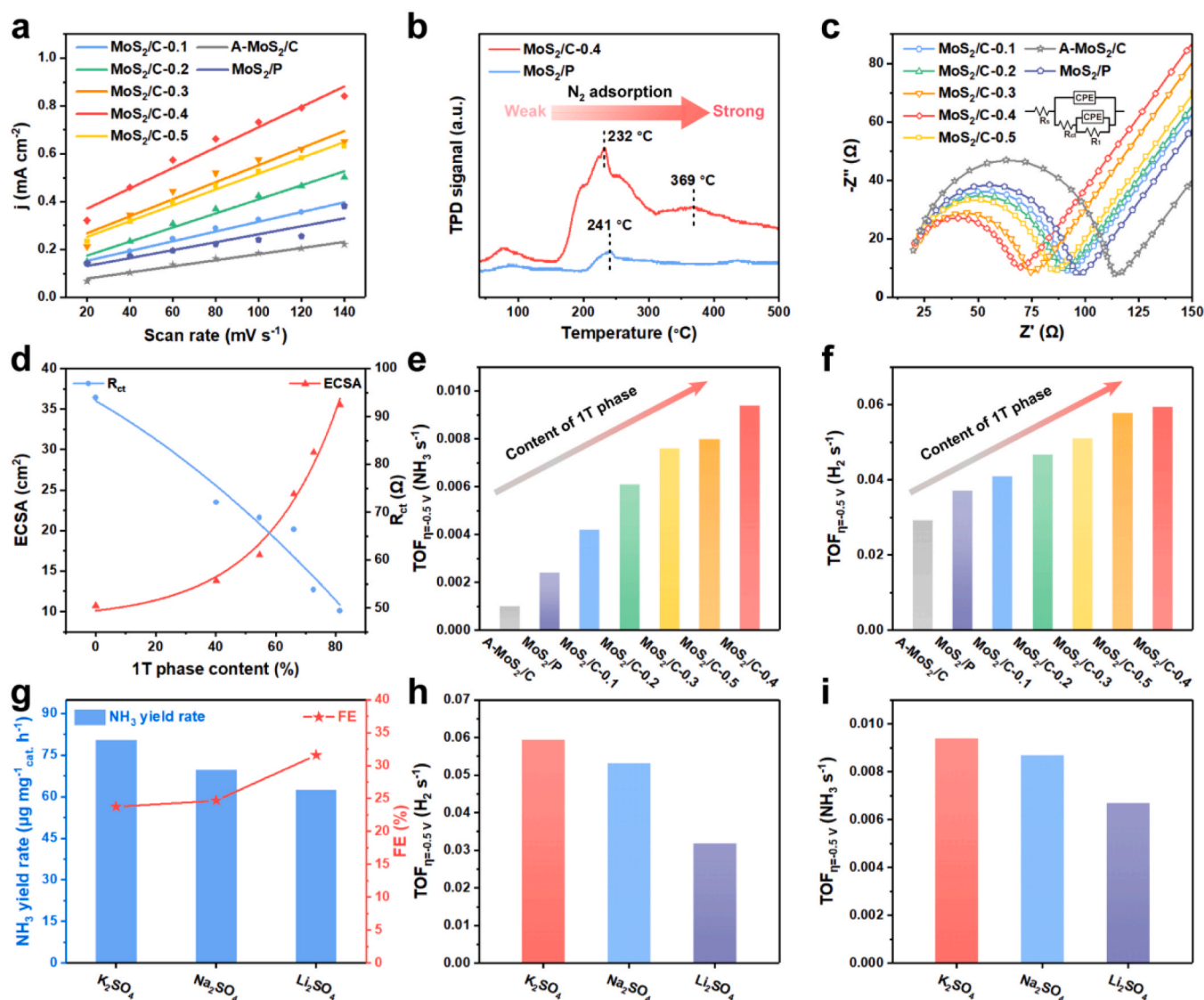
Fig. 5. (a) Measured capacitive currents plotted as a function of scan rate of all the samples. (b) Nitrogen temperature-programmed desorption of MoS$_2$/C-0.4 and MoS$_2$/P. (c) Electrochemical impedance spectroscopy spectra of all the samples. (d) Evolution of the ECSA and R$_{ct}$ vs. the content of 1T phase. Evolution of (e) TOF$_{NRR}$ and (f) TOF$_{HER}$ over all the samples. (g) Comparison of properties over MoS$_2$/C-0.4 at −0.5 V vs. RHE in K$_2$SO$_4$, Na$_2$SO$_4$, and Li$_2$SO$_4$ solutions. Evolution of (h) TOF$_{NRR}$ and (i) TOF$_{HER}$ over MoS$_2$/C-0.4 in K$_2$SO$_4$, Na$_2$SO$_4$, and Li$_2$SO$_4$ solutions.

than 32% in the Li$_2$SO$_4$ solution, laterally demonstrating the active site separation and synergistic effect in the DFT calculations.

4. Conclusions

In a nutshell, we have theoretically predicted and then experimentally realized an optimized phase state in terms of active site separation and a new role-playing synergistic mechanism to boost NRR selectivity and activity. The optimized MoS$_2$/C-0.4 catalyst possesses an ultrahigh 1T phase content of 81.45% with the assistance of a proper glucose additive and exhibits a high NH$_3$ yield rate of 80.38 µg h^{-1} mg$_{cat.}^{-1}$ and a large FE of 23.76% at −0.5 V vs. RHE, which is sixfold superior to those of A-MoS$_2$/C with pure 2H phase and surpasses almost all reported MoS$_2$-based electrocatalysts, suggesting the encouraging role-playing of phase engineering on NRR performances. Both experimental and theoretical evidence illustrates that the NRR performance enhancement of MoS$_2$/C-0.4 can be divided into three stages: (1) The NRR activity can be enhanced by the 1T phase due to the strengthened N$_2$ adsorption and boosted electron transfer capacity; (2) The NRR selectivity can be synchronously improved by the weakened competitive adsorption between

H$^+$ and N$_2$ reactant because of the active site separation; (3) The NRR process can be further boosted by the new role-playing synergistic mechanism that the basal plane with H$^+$ selective adsorption can provide a fundamental role in the NRR process as the H-provider to accelerate the hydrogenation steps. The present study demonstrates a promising strategy for active site separation and its further synergistic mechanism to synchronously improve the selectivity and activity toward NRR.

CRediT authorship contribution statement

Ruoqi Liu: Methodology, Investigation, Data curation, Formal analysis, Visualization, Writing-Original Draft. **Hao Fei:** Investigation, Formal analysis, Writing-Review & Editing. **Jian Wang:** Writing-Review & Editing. **Ting Guo:** Investigation, Software, Formal analysis, Writing-Review & Editing. **Fangyang Liu:** Writing-Review & Editing. **Jiayi Wang:** Investigation. **Zhuangzhi Wu:** Conceptualization, Writing-Review & Editing, Supervision. **Dezhi Wang:** Supervision.

Declaration of Competing Interest

The authors declare that they have no known competing financial interests or personal relationships that could have appeared to influence the work reported in this paper.

Data Availability

Data will be made available on request.

Acknowledgment

Appendix A. Supporting information

Supplementary data associated with this article can be found in the online version at doi:10.1016/j.apcatb.2023.122997.

References

[1] N. Gruber, J. Galloway, An earth-system perspective of the global nitrogen cycle, Nature 451 (2008) 293–296.

[2] D.R. MacFarlane, P.V. Cherepanov, J. Choi, B.H.R. Suryanto, R.Y. Hodgetts, J. M. Bakker, F.M. Ferrero Vallana, A.N. Simonov, A roadmap to the ammonia economy, Joule 4 (2020) 1186–1205.

[3] Y. Liu, L. Wang, L. Chen, H. Wang, A.R. Jadhav, T. Yang, Y. Wang, J. Zhang, A. Kumar, J. Lee, V.Q. Bui, M.G. Kim, H. Lee, Unveiling the protonation kinetics-dependent selectivity in nitrogen electroreduction: achieving 75.05% selectivity, Angew. Chem. Int. Ed. 61 (2022), e202209555.

[4] W.T. Wei, Z.J. Guo, J.Q. Xu, Z. Fang, J.J. Zhang, Y. Jia, L.W. Mi, Novel Ni₃S₄/NiS/ NC composite with multiple heterojunctions synthesized through space-confined effect for high-performance supercapacitors, in: Int. J. Extrem. Manuf, 5, 2023, 015504.

[5] Z.J. Guo, W.T. Wei, J. Shi, P.P. Wang, Z.S. Ye, L.W. Mi, NiS₂ nanoparticles by the NaCl-assisted less-liquid reaction system for the magnesium-ion battery cathode, Nanoscale 15 (2023) 1702–1708.

[6] W.T. Wei, J.R. Wu, S.Z. Cui, Y.M. Zhao, W.H. Chen, L.W. Mi, α-Ni(OH)₂/NiS₁.₉₇ heterojunction composites with excellent ion and electron transport properties for advanced supercapacitors, Nanoscale 11 (2019) 6243–6253.

[7] G.X. Lin, Q.J. Ju, X.W. Guo, W. Zhao, S. Adimi, J.Y. Ye, Q.Y. Bi, J.C. Wang, M. H. Yang, F.Q. Huang, Intrinsic electron iocalization of metastable MoS₂ boosts electrocatalytic nitrogen reduction to ammonia, Adv. Mater. 33 (2021), 2007509.

[8] J. Zhang, X.Y. Tian, M.J. Liu, H. Guo, J.D. Zhou, Q.Y. Fang, Z. Liu, Q. Wu, J. Lou, Cobalt-modulated molybdenum-dinitrogen interaction in MoS₂ for catalyzing ammonia synthesis, J. Am. Chem. Soc. 141 (2019) 19269–19275.

[9] T.F. Jaramillo, K.P. Jørgensen, J. Bonde, J.H. Nielsen, S. Horch, I. Chorkendorff, Identification of active edge sites for electrochemical H₂ evolution from MoS₂ nanocatalysts, Science 317 (2007) 100–102.

[10] Y. Yu, G.H. Nam, Q. He, X.J. Wu, K. Zhang, Z. Yang, J. Chen, Q. Ma, M. Zhao, Z. Liu, F.R. Ran, X. Wang, H. Li, X. Huang, B. Li, Q. Xiong, Q. Zhang, Z. Liu, L. Gu, Y. Du, W. Huang, H. Zhang, High phase-purity 1T′-MoS₂- and 1T′-MoSe₂-layered crystals, Nat. Chem. 10 (2018) 638–643.

[11] X.S. Xu, X.J. Tian, B.T. Sun, Z.Q. Liang, H.Z. Cui, J. Tian, M.H. Shao, 1 T-phase molybdenum sulfide nanodots enable efficient electrocatalytic nitrogen fixation under ambient conditions, Appl. Catal. B 272 (2020), 118984.

[12] X.S. Xu, B.T. Sun, Z.Q. Liang, H.Z. Cui, J. Tian, High-performance electrocatalytic conversion of N₂ to NH₃ using 1T′-MoS₂ anchored on Ti₃C₂ MXene under ambient conditions, ACS Appl. Mater. Interfaces 12 (2020) 26060–26067.

[13] X.R. Zi, J. Wan, X.H. Yang, W. Tian, H.J. Zhang, Y. Wang, Vacancy-rich 1T-MoS₂ monolayer confined to MoO₃ matrix: an interface-engineered hybrid for efficiently electrocatalytic conversion of nitrogen to ammonia, Appl. Catal. B 286 (2021), 119870.

[14] G.L. Fan, W.C. Xu, J.H. Li, J.L. Chen, M. Yu, Y.X. Ni, S.L. Zhu, X.C. Su, F.Y. Cheng, Nanoporous NiSb to enhance nitrogen electroreduction via tailoring competitive adsorption sites, Adv. Mater. 33 (2021) 2101126.

[15] R.Q. Liu, T. Guo, H. Fei, Z.Z. Wu, D.Z. Wang, F.Y. Liu, Highly efficient electrocatalytic N₂ reduction to ammonia over metallic 1T phase of MoS₂ enabled by active sites separation mechanism, Adv. Sci. 9 (2022), 2103583.

[16] Y.Y. Ma, T. Yang, H.Y. Zou, W.J. Zang, Z.K. Kou, L. Mao, Y.P. Feng, L. Shen, S. J. Pennycook, L.L. Duan, X. Li, J. Wang, Synergizing Mo single atoms and Mo₂C nanoparticles on CNTs synchronizes selectivity and activity of electrocatalytic N₂ reduction to ammonia, Adv. Mater. 32 (2020), 2002177.

[17] D. Voiry, M. Salehi, R. Silva, T. Fujita, M. Chen, T. Asefa, V.B. Shenoy, G. Eda, M. Chhowalla, Conducting MoS₂ nanosheets as catalysts for hydrogen evolution reaction, Nano Lett. 13 (2013) 6222–6227.

[18] Y. Yin, J. Han, Y. Zhang, X. Zhang, P. Xu, Q. Yuan, L. Samad, X. Wang, Y. Wang, Z. Zhang, P. Zhang, X. Cao, B. Song, S. Jin, Contributions of phase, sulfur vacancies, and edges to the hydrogen evolution reaction catalytic activity of porous molybdenum disulfide nanosheets, J. Am. Chem. Soc. 138 (2016) 7965–7972.

[19] B.H.R. Suryanto, D.B. Wang, L.M. Azofra, M. Harb, L. Cavallo, R. Jalili, D.R. G. Mitchell, M. Chatti, D.R. MacFarlane, MoS₂ polymorphic engineering enhances selectivity in the electrochemical reduction of nitrogen to ammonia, ACS Energy Lett. 4 (2019) 430–435.

[20] J. Bai, B.Z. Zhao, J.F. Zhou, J.G. Si, Z.T. Fang, K.Z. Li, H.Y. Ma, J.M. Dai, X.B. Zhu, Y.P. Sun, Glucose-induced synthesis of 1T-MoS₂/C hybrid for high-rate lithium-ion batteries, Small 15 (2019), 1805420.

[21] H. Jiang, D. Ren, H. Wang, Y. Hu, S. Guo, H. Yuan, P. Hu, L. Zhang, C. Li, 2D monolayer MoS₂-carbon interoverlapped superstructure: engineering ideal atomic interface for lithium ion storage, Adv. Mater. 27 (2015) 3687.

[22] M. Acerce, D. Voiry, M. Chhowalla, Metallic 1T phase MoS₂ nanosheets as supercapacitor electrode materials, Nat. Nanotechnol. 10 (2015) 313–318.

[23] H. Fei, T. Guo, Y. Xin, L.B. Wang, R.Q. Liu, D.Z. Wang, F.Y. Liu, Z.Z. Wu, Sulfur vacancy engineering of MoS₂ via phosphorus incorporation for improved electrocatalytic N₂ reduction to NH₃, Appl. Catal. B 300 (2022), 120733.

[24] Z. Sun, Y. Yao, J. Wang, X. Song, P. Zhang, L. Zhao, L. Gao, High rate lithium-ion batteries from hybrid hollow spheres with a few-layered MoS₂-entrapped carbon sheath synthesized by a space-confined reaction, J. Mater. Chem. A 4 (2016) 10425–10434.

[25] S.S. Chou, N. Sai, P. Lu, E.N. Coker, S. Liu, K. Artyushkova, T.S. Luk, B. Kaehr, C. J. Brinker, Understanding catalysis in a multiphasic two-dimensional transition metal dichalcogenide, Nat. Commun. 6 (2015) 8311.

[26] K. Le, X. Zhang, Q. Zhao, Y.Z. Liu, P. Yi, S.S. Xu, W.M. Liu, Controllably doping nitrogen into 1T/2H MoS₂ heterostructure nanosheets for enhanced supercapacitive and electrocatalytic performance by low-power N₂ plasma, ACS Appl. Mater. Interfaces 13 (2021) 44427–44439.

[27] Q. Liu, X. Li, Q. He, A. Khalil, D. Liu, T. Xiang, X. Wu, L. Song, Gram-scale aqueous synthesis of stable few-layered 1T-MoS₂: applications for visible-light-driven photocatalytic hydrogen evolution, Small 11 (2015) 5556–5564.

[28] J.Y. Wang, J. Tang, J. Guo, S.H. Zhang, W. Xi, H.B. Tan, Y. Bando, X. Wang, Y. Yamauchi, C₃N₄-digested 3D construction of hierarchical metallic phase MoS₂ nanostructures, J. Mater. Chem. A 7 (2019) 18388–18396.

[29] X. Geng, W. Sun, W. Wu, B. Chen, A. Al-Hilo, M. Benamara, H. Zhu, F. Watanabe, J. Cui, T.P. Chen, Pure and stable metallic phase molybdenum disulfide nanosheets for hydrogen evolution reaction, Nat. Commun. 7 (2016) 10672.

[30] H. Li, S. Chen, X. Jia, B. Xu, H. Lin, H. Yang, L. Song, X. Wang, Amorphous nickel-cobalt complexes hybridized with 1T-phase molybdenum disulfide via hydrazine-induced phase transformation for water splitting, Nat. Commun. 8 (2017) 15377.

[31] D.Z. Wang, X.Y. Zhang, S.Y. Bao, Z.T. Zhang, H. Fei, Z.Z. Wu, Phase engineering of a multiphasic 1T/2H MoS₂ catalyst for highly efficient hydrogen evolution, J. Mater. Chem. A 5 (2017) 2681–2688.

[32] X.B. Fan, P.T. Xu, D.K. Zhou, Y.F. Sun, Y.G.C. Li, M.A.T. Nguyen, M. Terrones, T. E. Mallouk, Fast and efficient preparation of exfoliated 2H MoS₂ nanosheets by sonication-assisted lithium intercalation and infrared laser-induced 1T to 2H phase reversion, Nano Lett. 15 (2015) 5956–5960.

[33] Z.Q. Xie, S.L. Yu, X.H. Ma, K. Li, L. Ding, W.T. Wang, D.A. Cullen, H.M. Meyer, H. R. Yu, J.H. Tong, Z.L. Wu, F.Y. Zhang, MoS₂ nanosheet integrated electrodes with engineered ¹T–²H phases and defects for efficient hydrogen production in practical PEM electrolysis, Appl. Catal. B 313 (2022), 121458.

[34] P.A. Bertrand, Surface-phonon dispersion of MoS₂, Phys. Rev. B 44 (1991) 5745.

[35] X.Y. Chia, A. Ambrosi, Z. Sofer, J. Luxa, M. Pumera, Catalytic and charge transfer properties of transition metal dichalcogenides arising from electrochemical pretreatment, ACS Nano 9 (2015) 5164–5179.

[36] Y.H. Lee, K. Liu, X.P. Hong, M. Chen, J. Kim, S.F. Shi, J.Q. Wu, A. Zettl, F. Wang, Probing local strain at MX₂-metal boundaries with surface plasmon-enhanced Raman scattering, Nano Lett. 14 (2014) 5329–5334.

[37] J. Zhang, M.H. Wu, Z.T. Shi, M. Jiang, W.J. Jian, Z. Xiao, J. Li, C.S. Lee, J. Xu, Composition and interface engineering of alloyed MoS₂ₓSe₂(₁₋ₓ) nanotubes for enhanced hydrogen evolution reaction activity, Small 12 (2016) 4379–4385.

[38] P. Hao, Z.H. Zhao, Y.H. Leng, J. Tian, Y.H. Sang, R.I. Boughton, C.P. Wong, H. Liu, B. Yang, Graphene-based nitrogen self-doped hierarchical porous carbon aerogels derived from chitosan for high performance supercapacitors, Nano Energy 15 (2015) 9–23.

[39] K. Chang, X. Hai, H. Pang, H.B. Zhang, L. Shi, G.G. Liu, H.M. Liu, G.X. Zhao, M. Li, J.H. Ye, Targeted synthesis of 2H- and 1T-phase MoS₂ monolayers for catalytic hydrogen evolution, Adv. Mater. 28 (2016) 10033.

[40] B. Vedhanarayanan, J. Shi, J.Y. Lin, S.N. Yun, T.W. Lin, Enhanced activity and stability of MoS₂ through enriching 1T-phase by covalent functionalization for energy conversion applications, Chem. Eng. J. 403 (2021), 126318.

[41] Y.C. Lin, D.O. Dumcenco, Y.S. Huang, K. Suenaga, Atomic mechanism of the semiconducting-to-metallic phase transition in single-layered MoS₂, Nat. Nanotechnol. 9 (2014) 391–396.

[42] Y.G. Yin, S.T. Wei, L. Zhang, Z.W. Guo, H.H. Huang, S.R. Sai, J.D. Wu, Y.C. Xu, Y. Liu, L.R. Zheng, X.F. Fan, X.Q. Cui, Copper-linked 1T MoS₂/Cu₂O heterostructure for efficient photocatalytic hydrogen evolution, Chem. Res. Chin. Univ. 36 (2020) 1122–1127.

[43] D.Y. Chung, S. Keun Park, Y.H. Chung, S.H. Yu, D.H. Lim, N. Jung, H.C. Ham, H. Y. Park, Y.Z. Piao, S.J. Yoo, Y.E. Sung, Edge-exposed MoS₂ nano-assembled structures as efficient electrocatalysts for hydrogen evolution reaction, Nanoscale 6 (2014) 2131–2136.

[44] Z.Q. Liu, K.K. Nie, X.Y. Qu, X.H. Li, B.J. Li, Y.L. Yuan, S.K. Chong, P. Liu, Y.G. Li, Z. Y. Yin, W. Huang, General bottom-up colloidal synthesis of nano-monolayer transition-metal dichalcogenides with high 1T′-phase purity, J. Am. Chem. Soc. 11 (2022) 4863–4873.

[45] H. Fei, R.Q. Liu, J. Wang, T. Guo, Z.Z. Wu, D.Z. Wang, F.Y. Liu, Targeted modulation of competitive active sites toward nitrogen fixation via sulfur vacancy engineering over MoS$_2$, Adv. Funct. Mater. (2023), 2302501.

[46] M.F. Wang, S.S. Liu, H.Q. Ji, T.Z. Yang, T. Qian, C.L. Yan, Salting-out effect promoting highly efficient ambient ammonia synthesis, Nat. Commun. 12 (2021) 3198.

[47] B.H.R. Suryanto, H.L. Du, D.B. Wang, J. Chen, A.N. Simonov, D.R. MacFarlane, Challenges and prospects in the catalysis of electroreduction of nitrogen to ammonia, Nat. Catal. 2 (2019) 290–296.

[48] P. Li, Z. Jin, Z. Fang, G. Yu, A surface-strained and geometry-tailored nanoreactor that promotes ammonia electrosynthesis, Angew. Chem. Int. Ed. 59 (2020) 22610–22616.

[49] Y. Kong, Y. Li, X.H. Sang, B. Yang, Z.J. Li, S.X. Zheng, Q.H. Zhang, S.Y. Yao, X. X. Yang, L.C. Lei, S.D. Zhou, G. Wu, Y. Hou, Atomically dispersed zinc[I] active sites to accelerate nitrogen reduction kinetics for ammonia electrosynthesis, Adv. Mater. 34 (2021), 2103548.

[50] H.Y. Su, L.L. Chen, Y.Z. Chen, R. Si, Y.T. Wu, X.N. Wu, Z.G. Geng, W.H. Zhang, J. Zeng, Single atoms of iron on MoS$_2$ nanosheets for N$_2$ electroreduction into ammonia, Angew. Chem. Int. Ed. 59 (2020) 20411–20416.

[51] Y. Li, Y.X. Ji, Y.J. Zhao, J.X. Chen, S.X. Zheng, X.H. Sang, B. Yang, Z.J. Li, L.C. Lei, Z.H. Wen, X.L. Feng, Y. Hou, Local spin-state tuning of iron single-atom electrocatalyst by S-coordinated doping for kinetics-boosted ammonia synthesis, Adv. Mater. 34 (2022), 2202240.

[52] M.D. Liu, S. Zhang, M. Chen, L.M. Wu, Boosting electrochemical nitrogen reduction performance through water-in-salt electrolyte, Appl. Catal. B 319 (2022), 121925.

[53] C.Q. Ma, Y.L. Zhang, S.H. Yan, B.P. Liu, Carbon-doped boron nitride nanosheets: a high-efficient electrocatalyst for ambient nitrogen reduction, Appl. Catal. B 315 (2022), 121574.

[54] L. Zhang, X.Q. Ji, X. Ren, Y.J. Ma, X.F. Shi, Z.Q. Tian, A.M. Asiri, L. Chen, B. Tang, X.P. Sun, Electrochemical ammonia synthesis via nitrogen reduction reaction on a MoS$_2$ catalyst: theoretical and experimental studies, Adv. Mater. 30 (2018), 1800191.

[55] X.H. Li, T.S. Li, Y.J. Ma, Q. Wei, W.B. Qiu, H.R. Guo, X.F. Shi, P. Zhang, A.M. Asiri, L. Chen, B. Tang, X.P. Sun, Boosted electrocatalytic N$_2$ reduction to NH$_3$ by defect-rich MoS$_2$ nanoflower, Adv. Energy Mater. 8 (2018), 1801357.

[56] C.Q. Ma, D. Liu, Y.L. Zhang, J.Y. Lee, J. Tian, B.P. Liu, S.H. Yan, MOF-derived Fe$_2$O$_3$@MoS$_2$: an efficient electrocatalyst for ammonia synthesis under mild conditions, Chem. Eng. J. 430 (2022), 132694.

[57] Y. Song, D. Johnson, R. Peng, D.K. Hensley, P.V. Bonnesen, L. Liang, J. Huang, F. Yang, F. Zhang, R. Qiao, A.P. Baddorf, T.J. Tschaplinski, N.L. Engle, M. C. Hatzell, Z. Wu, D.A. Cullen, H.M. Meyer III, B.G. Sumpter, A.J. Rondinone, A physical catalyst for the electrolysis of nitrogen to ammonia, Sci. Adv. 4 (2018), e1700336.